

# Charge-to-Spin Interconversion in Low-Symmetry Topological Materials

**Marc Vila**

Institut Català de Nanociència i Nanotecnologia

**Chuang-Han Hsu**

Institute of Physics, Academia Sinica, Taipei Taiwan <https://orcid.org/0000-0002-2394-8537>

**Jose Garcia Aguilar**

Catalan Institute of Nanoscience and Nanotechnology <https://orcid.org/0000-0002-5752-4759>

**Antonio Benitez**

Catalan Institute of Nanoscience and Nanotechnology (ICN2), CSIC and The Barcelona Institute of Science and Technology, Campus UAB, Bellaterra, 08193 Barcelona <https://orcid.org/0000-0003-1049-4983>

**Xavier Waintal**

CEA Grenoble

**Sergio Valenzuela**

Catalan Institute of Nanoscience and Nanotechnology (ICN2) <https://orcid.org/0000-0002-4632-8891>

**Vitor Pereira**

National University of Singapore <https://orcid.org/0000-0002-3462-524X>

**Stephan Roche** (✉ [stephan.roche@icn2.cat](mailto:stephan.roche@icn2.cat))

Catalan Institute of Nanoscience and Nanotechnology (ICN2), CSIC and The Barcelona Institute of Science and Technology, Campus UAB, Bellaterra, 08193 Barcelona <https://orcid.org/0000-0003-0323-4665>

---

## Article

**Keywords:** spin Hall effect, Weyl semimetals, transition metal dichalcogenides, spin relaxation, persistent spin texture, quantum transport

**Posted Date:** January 6th, 2021

**DOI:** <https://doi.org/10.21203/rs.3.rs-124172/v1>

**License:**  This work is licensed under a Creative Commons Attribution 4.0 International License.

[Read Full License](#)

---

# Charge-to-Spin Interconversion in Low-Symmetry Topological Materials

Marc Vila,<sup>\*,†,‡</sup> Chuang-Han Hsu,<sup>¶,§</sup> Jose H. Garcia,<sup>†</sup> L. Antonio Benítez,<sup>†,‡</sup>  
Xavier Waintal,<sup>||</sup> Sergio O. Valenzuela,<sup>†,⊥</sup> Vitor M. Pereira,<sup>§,#</sup> and Stephan  
Roche<sup>\*,†,⊥</sup>

<sup>†</sup>*Catalan Institute of Nanoscience and Nanotechnology (ICN2), CSIC and BIST, Campus  
UAB, Bellaterra, 08193 Barcelona, Spain*

<sup>‡</sup>*Department of Physics, Universitat Autònoma de Barcelona, Campus UAB, Bellaterra,  
08193 Barcelona, Spain*

<sup>¶</sup>*Department of Electrical and Computer Engineering, National University of Singapore,  
Singapore 117576, Singapore*

<sup>§</sup>*Centre for Advanced 2D Materials and Graphene Research Centre, National University of  
Singapore, Singapore 117546, Singapore*

<sup>||</sup>*Univ. Grenoble Alpes, CEA, IRIG-PHELIQS, 38000 Grenoble, France*

<sup>⊥</sup>*ICREA–Institució Catalana de Recerca i Estudis Avançats, 08010 Barcelona, Spain*

<sup>#</sup>*Department of Materials Science and Engineering, National University of Singapore,  
Singapore 117575*

E-mail: [marc.vila@icn2.cat](mailto:marc.vila@icn2.cat); [stephan.roche@icn2.cat](mailto:stephan.roche@icn2.cat)

## Abstract

The spin polarization induced by the spin Hall effect (SHE) in thin films typically points out of the plane. This is rooted on the specific symmetries of traditionally

5 studied systems, not in a fundamental constraint. Here, we show that the reduced  
6 symmetry of strong spin-orbit coupling materials such as MoTe<sub>2</sub> or WTe<sub>2</sub> enables a  
7 new form of *canted* spin Hall effect (SHE), characterized by large and robust *in-plane*  
8 spin polarizations, which gives rise to an unprecedented charge-to-spin interconversion  
9 effect. Through quantum transport calculations on realistic device geometries, includ-  
10 ing disorder, we found long spin diffusion lengths ( $\lambda_s$ ) and a gate tunable charge-to-spin  
11 interconversion efficiency with an upper value reaching  $\theta_{xy} \approx 80\%$ . The SHE figure of  
12 merit  $\lambda_s \theta_{xy} \sim 1\text{--}50$  nm, can significantly exceed values of conventional SHE materi-  
13 als, and stems from momentum-invariant (persistent) spin textures together with large  
14 spin Berry curvature along the Fermi contour. Specific guidelines for unambiguous  
15 experimental confirmation are proposed, paving the way towards exploiting such phe-  
16 nomena in spintronic devices. These findings vividly emphasize how crystal symmetry  
17 and band topology can govern the intrinsic SHE, and how they may be exploited to  
18 broaden the range and efficiency of spintronic functionalities.

19 **Keywords:** spin Hall effect, Weyl semimetals, transition metal dichalcogenides, spin  
20 relaxation, persistent spin texture, quantum transport.

21 Unconventional manifestations of spin-orbit coupling (SOC) are rapidly extending the  
22 ability to generate, control and carry spin polarization for applications of spin transport or  
23 spin-driven magnetic torques beyond conventional spintronic materials.<sup>1-4</sup> Topological ma-  
24 terials form a natural family to scrutinize in this regard: their key features often derive  
25 from a large SOC combined with band inversions, and their topologically protected surface  
26 states may prove instrumental to enable coherent, dissipationless spin currents over long-  
27 distances.<sup>5,6</sup> 3D Weyl semimetals (WSM) are defined by the presence of band degeneracy  
28 points near the Fermi energy ( $E_F$ ) with local linear dispersion in all directions.<sup>7,8</sup> Layered  
29 transition metal dichalcogenides (TMDs) in the 1T' ( $P2_1/m$ ) or 1T<sub>d</sub> ( $Pmn2_1$ ) phases ac-  
30 commodate the interesting class of WSM candidates MX<sub>2</sub> (M = Mo, W; X = S, Se, Te), which  
31 have been advanced as platforms for realizing exotic phenomena such as topological su-

32 perconductivity,<sup>9–12</sup> axion-field-enabled nonreciprocal thermal radiation,<sup>13</sup> anisotropic spin  
33 Hall transport<sup>14</sup> or out-of-plane spin-orbit torque.<sup>15,16</sup> When thinned towards the monolayer  
34 limit, they transition from the type-II WSM bulk phase to the quantum spin Hall regime<sup>17–31</sup>  
35 with strain-tunable topological gap.<sup>32</sup>

36 Recently, large charge-to-spin interconversion (CSI) generated by the spin Hall effect  
37 (SHE) has been reported in multilayers of MoTe<sub>2</sub> and WTe<sub>2</sub><sup>33–36</sup> with evidence of long spin  
38 diffusion lengths ( $\lambda_s$ ).<sup>34</sup> The efficiency of the SHE is characterized by the spin Hall angle  
39 (SHA,  $\theta_{xy}$ ) which indicates which fraction of a driving charge current can be converted into  
40 spin current;  $\theta_{xy}$  depends on the magnitude of SOC and is typically no more than a few  
41 percent at room temperature in heavy metals.<sup>37</sup> In traditional SHE materials, the stronger  
42 the SOC, the shorter  $\lambda_s$  is; consequently, achieving long  $\lambda_s$  concurrently with large SHA is  
43 a long-standing challenge for spintronics. To date, the best tradeoff obtained with heavy  
44 metals amounts to  $\lambda_s\theta_{xy} \sim 0.1\text{--}0.2$  nm.<sup>37–41</sup> Interestingly, hints of unconventional SHE have  
45 been detected in 1T'<sup>33</sup> and 1T<sub>d</sub> phases of MoTe<sub>2</sub> multilayers.<sup>34</sup> On general terms, such  
46 unconventional spintronic response is possible because, in contrast to bulk crystals with T<sub>d</sub>  
47 structure, the absence of the glide mirror symmetry in few-layer slabs is expected to generate  
48 additional non-zero components of the spin Hall conductivity (SHC) tensor,<sup>42</sup> resulting in  
49 spin current with polarization collinear with the charge current. Additionally, the higher  
50 structural quality and resilience to disorder of topological materials such as MoTe<sub>2</sub> or WTe<sub>2</sub>  
51 should favor larger SHE efficiency primarily driven by a strong SOC and intrinsic SHC.  
52 However, to date, the underlying theoretical mechanism at play in these systems, as well as  
53 its impact on  $\lambda_s\theta_{xy}$ , remain to be clarified.

54 Here, we show that unique symmetry-induced spin textures of electronic states in MoTe<sub>2</sub>  
55 and WTe<sub>2</sub> monolayers yield *a giant* canted SHE where the spin current polarization lies in the  
56  $yz$  plane. We obtained CSI efficiencies as high as 80% and values of  $\lambda_s$  in the range 10–100  
57 nm; the latter is up to one order of magnitude larger than in heavy metals with similar spin  
58 Hall efficiency.<sup>37</sup> These results are a direct consequence of: (i) the persistent (momentum-

59 invariant) spin texture observed with DFT; and (ii) a large spin Berry curvature stemming  
60 from the band inversion and hybridization near  $E_F$  that underlies the nontrivial topology of  
61 these monolayers. Moreover, all spin transport characteristics are gate-tunable, being max-  
62 imal near the band edge. Our findings hinge on a density functional theory (DFT)-derived  
63 effective tight-binding model deployed in spintronic simulations using state-of-the-art quan-  
64 tum transport methodologies. While there have been recent theoretical characterizations of  
65 the SHC in pristine forms of these materials,<sup>14,34</sup> deeper understanding of the spin dynamics  
66 and transport remains pressing, and realistic assessment of spin transport length scales is  
67 paramount for further experimental scrutiny and practical applications. We address those  
68 questions here.

We computed the bandstructures of  $1T'$ - and  $1T_d$ -derived monolayers of  $\text{MoTe}_2$  and  $\text{WTe}_2$  within DFT (see Supporting Information<sup>43</sup>). Effective Hamiltonians based on maximally localized Wannier functions were subsequently extracted, allowing straightforward computation of the SHC and spin textures with no intervening approximations. Yet, such Hamiltonian is still too complex to be efficiently deployed in large-scale transport calculations on system sizes involving millions of unit cells. We therefore built a  $\mathbf{k} \cdot \mathbf{p}$  Hamiltonian to describe the two conduction and two valence bands nearest  $E_F$  which, at the  $\Gamma$  point, respectively transform according to the representations  $B_u$  (valence) and  $A_g$  (conduction) of the  $C_{2h}$  point group.<sup>19</sup> Extension of the symmetry-allowed  $\mathbf{k} \cdot \mathbf{p}$  terms to the full Brillouin

zone yields the following nearest-neighbor tight-binding representation:<sup>43</sup>

$$\begin{aligned}
H = & \sum_{i,s} (\Delta + 4m_p + \delta) c_{i,s}^\dagger c_{i,s} \\
& - \sum_{\langle ij \rangle, s} (m_p + m_d) c_{i,s}^\dagger c_{j,s} \\
& + \sum_{i,s} (\Delta - 4m_d - \delta) d_{i,s}^\dagger d_{i,s} \\
& - \sum_{\langle ij \rangle, s} (m_p - m_d) d_{i,s}^\dagger d_{j,s} \\
& - \sum_{\langle ij \rangle, s} \frac{\beta}{2} (\hat{\mathbf{l}}_{ij} \cdot \hat{\mathbf{y}}) c_{i,s}^\dagger d_{j,s} + \sum_{i,s} \eta c_{i,s}^\dagger d_{i,s} \\
& - \sum_{\langle ij \rangle} \sum_{ss'} \frac{i}{2} (\mathbf{\Lambda}_{ss'} \times \hat{\mathbf{l}}_{ij}) \cdot (\hat{\mathbf{y}} + \hat{\mathbf{z}}) c_{i,s}^\dagger d_{j,s'}. \tag{1}
\end{aligned}$$

69 This is an effective 4-band Hamiltonian generated by two orbitals (plus spin) per unit cell on  
70 a rectangular lattice, one arising from the chalcogen  $p_y$  states and the other from metal  $d_{yz}$   
71 orbitals, respectively associated with the  $c_{i,s}$  and  $d_{i,s}$  operators at each unit cell  $i$  ( $s$  labels  
72 the spin projection). The first four terms in Eq. (1) describe spin-degenerate valence and  
73 conduction bands with hopping amplitudes set by  $m_p \pm m_d$ ,  $\delta$  parameterizes the degree of  
74 band inversion at  $\Gamma$ , and a constant  $\Delta$  is used to match the position of the conduction band  
75 and  $E_F$  with those obtained by DFT. In the fifth term,  $\beta$  accounts for the  $x$ - $y$  crystalline  
76 anisotropy, with  $\hat{\mathbf{l}}_{ij}$  a unit vector pointing from site  $i$  to  $j$ ; the term  $\propto \eta$  breaks inversion  
77 symmetry and determines, for example, whether we are describing a monolayer descended  
78 from a 1T' ( $\eta = 0$ ) or 1T<sub>d</sub> bulk crystal. The last term embodies the SOC, where  $\mathbf{\Lambda} \equiv$   
79  $(\Lambda_x \sigma_x, -\Lambda_y \sigma_y, \Lambda_z \sigma_z)$ ,  $\sigma_{x,y,z}$  are the spin Pauli matrices and  $\hat{\mathbf{y}}, \hat{\mathbf{z}}$  are unit Cartesian vectors.  
80 The parameters are set by fitting the energy dispersion and spin texture to the ones obtained  
81 by DFT.<sup>43</sup> To be specific, we henceforth concentrate on the case of MoTe<sub>2</sub>, as it is the  
82 one where experiments have recently reported in-plane SHE.<sup>33,34</sup> Nonetheless, because the  
83 Hamiltonian model (1) captures equally well the case of WTe<sub>2</sub> and similar low-symmetry

84 TMDs,<sup>43</sup> qualitatively comparable results can be expected in those monolayers as well. Since  
 85 the DFT calculations show that MoTe<sub>2</sub> is slightly *n*-doped, we favored the conduction band  
 86 in the fits and will focus exclusively on cases where  $E_F$  lies in the conduction band.

87 The band structure near  $E_F$  is shown in Fig. 1a. The valence and conduction extrema  
 88 occur at the time-reversal-symmetric Q points; the small splitting arises from the small  
 89 inversion-symmetry-breaking ( $\eta \neq 0$ ) that occurs in monolayers derived from the T<sub>d</sub> bulk  
 90 structure. Since this work focuses on the scenario where  $E_F$  lies in the conduction band,  
 91 the figure shows a closeup of the conduction electron pockets; the full DFT bandstructure  
 92 and the  $\mathbf{k} \cdot \mathbf{p}$  fit are discussed in the Supporting Information.<sup>43</sup> Fig. 1b shows the spin  
 93 texture at the Fermi energy,  $\langle s^\alpha \rangle_{E_F}$ , with two crucial observations: the existence of an  
 94 approximate *persistent spin texture* through the whole Fermi contour<sup>44–46</sup> and canted spins  
 95 with  $\langle s^y \rangle_{E_F} \gtrsim \langle s^z \rangle_{E_F} \gg \langle s^x \rangle_{E_F}$ , consistent with prior studies.<sup>47,48</sup>

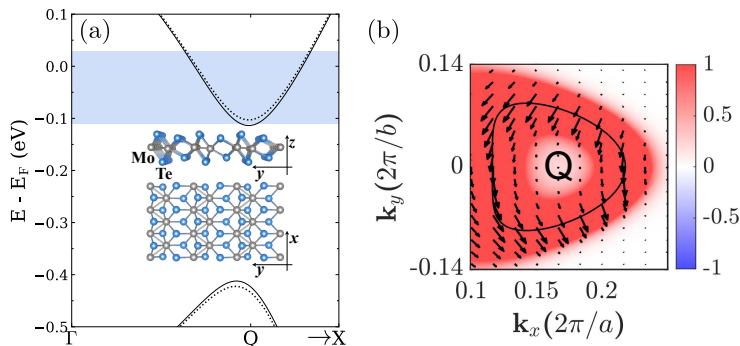


Figure 1: (a) Close-up of the bandstructure near  $E_F$  for a T<sub>d</sub>-MoTe<sub>2</sub> monolayer (model of Eq. (1)). The blue-shaded region indicates the energy range covered in the spin transport calculations. Inset: monolayer crystal structure. (b) Spin texture of one of the bands of the electron pocket near Q at  $E_F$  (Fermi-broadened with  $T = 300$  K); the solid line marks the Fermi contour, arrows depict the in-plane spin projection and the color indicates the spin projection along  $z$ .

96 We explored the spin transport properties using linear response theory and the Landauer-  
 97 Büttiker formalism as implemented in Kwant.<sup>49</sup> We simulated the nonlocal spin valve illus-  
 98 trated in the inset of Fig. 2, where contacts 2 and 3 are ferromagnetic (FM) to allow injection  
 99 and detection of spin-polarized currents:<sup>50–52</sup> FM electrode 2 injects a spin-polarized current  
 100  $I_0^\alpha$  with spins polarized along  $\alpha \in \{x, y, z\}$ ; this creates a spin accumulation that diffuses

101 along the channel and is detected as a nonlocal voltage  $V_{\text{nl}}$  at electrodes 3-4, located a dis-  
 102 tance  $L$  from the source and far from the path of charge current between electrodes 1-2. This  
 103 effect is quantified by the nonlocal resistance  $R_{\text{nl}}^\alpha \equiv V_{\text{nl}}/I_0^\alpha$ . The spin diffusion length for  
 104  $\alpha$ -pointing spins,  $\lambda_s^\alpha$ , is obtained from the decay of  $R_{\text{nl}}^\alpha$  with  $L$  in the diffusive regime (mean  
 105 free path shorter than  $L$ ). To ensure our results reflect the diffusive regime, we add Anderson  
 106 disorder to the Hamiltonian and extract statistics only within the appropriate scaling region  
 107 of the device conductance.<sup>43,53</sup>

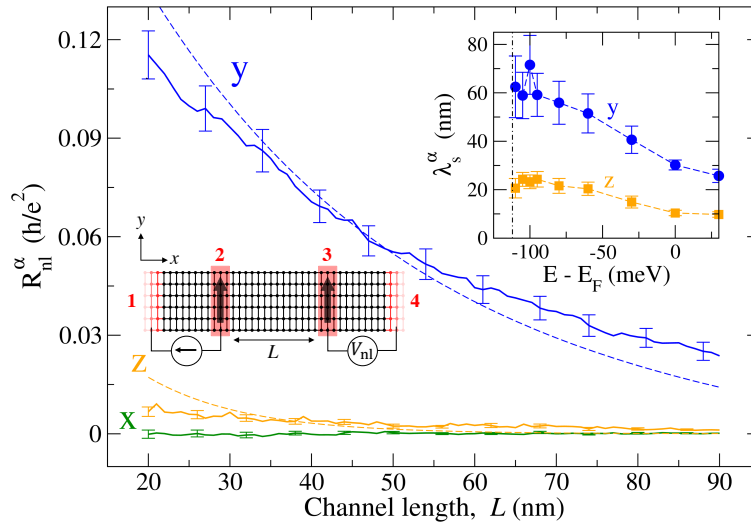


Figure 2:  $R_{\text{nl}}^\alpha$  (solid lines) against the channel length,  $L$ , for spins polarized along  $x$ ,  $y$  and  $z$ . Error bars result from averaging over 150 disorder configurations ( $w = 50$  nm). Dashed lines are fits to Eq. (6) in.<sup>43</sup> Left inset: Scheme of the nonlocal spin valve. Black (red) regions denote the device (leads), with leads 2 and 3 being ferromagnetic. Current  $I_0^\alpha$  flows from lead 2 to 1 and  $V_{\text{nl}}$  is measured between leads 3 and 4. Right inset: Energy-dependence of  $\lambda_s^{y,z}$ . The dot-dashed line marks the conduction band minimum.

108 Fig. 2 shows  $R_{\text{nl}}^\alpha(L)$  for the three spin orientations at  $E_F$ . We see clear differences in the  
 109 magnitude of the nonlocal signals and their relaxation distances for different orientations of  
 110 the injected spins, ranging from tens of nanometers to the sub-nanometer scale. By fitting  
 111 the length dependence of  $R_{\text{nl}}^\alpha$  to the solution of the spin diffusion equations (dashed lines in  
 112 Fig. 2),<sup>53</sup> we obtained  $\lambda_s^y \approx 30$  nm and  $\lambda_s^z \approx 10$  nm, while  $\lambda_s^x$  has a negligible value. These  
 113 values are comparable with strong-SOC metals such as Pt,  $\beta$ -W or  $\beta$ -Ta.<sup>37,39</sup> It is significant  
 114 that the spin diffusion lengths follow the trend  $\lambda_s^y \gtrsim \lambda_s^z \gg \lambda_s^x$ , in correspondence to that of

115 the spin texture around the Fermi contour at equilibrium. The upper inset of Fig. 2 shows  
 116 that this hierarchy holds over the entire range of energies analyzed, from  $E = 30$  meV to the  
 117 band edge at  $\sim -110$  meV (we measure energies relative to  $E_F$  of undoped  $\text{MoTe}_2$ ). Details  
 118 of how the (persistent) spin texture impacts  $\lambda_s^\alpha$  and its scaling with energy are discussed  
 119 in the Supporting Information.<sup>43</sup> Both  $\lambda_s^y$  and  $\lambda_s^z$  increase about threefold as  $E_F$  moves  
 120 towards the band edge (dot-dashed line). Moreover, we found that  $\lambda_s^y$  at  $E_F = -140$  meV  
 121 (in the band gap) increases up to  $\simeq 156$  nm, while deeper into the gap ( $E = -320$  meV)  
 122 we see no decay in the spin signal, consistent with the onset of ballistic regime where spin is  
 123 transported by topologically protected surface states.<sup>43</sup>

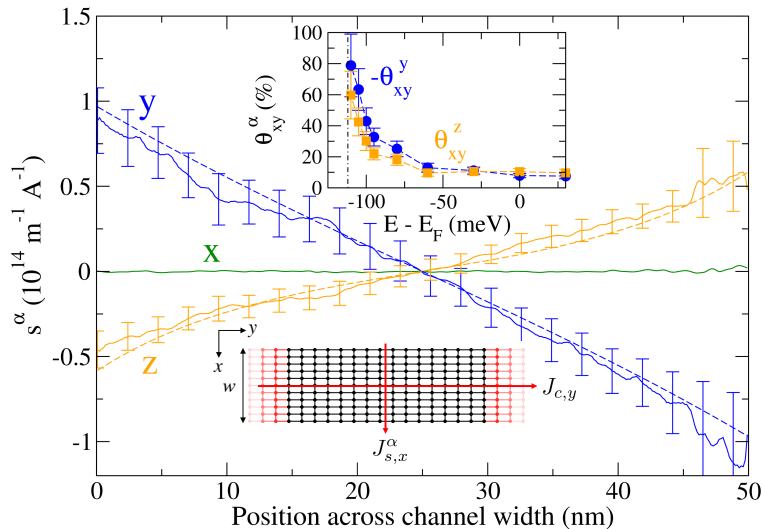


Figure 3: Spin accumulation (solid lines) as a function of position across the channel width, of spins along  $x$ ,  $y$  and  $z$ . Error bars result from averaging over 200 disorder configurations ( $w = 50$  nm). Dashed lines are fits to Eq. (2). Bottom inset: Scheme of the two-terminal device, where a current flowing along  $y$  creates a spin accumulation in the  $x$  direction. Top inset: Energy dependence of the spin Hall angles, with the conduction band minimum marked by a dot-dashed line.

124 The SHE was investigated by computing the spin accumulation and analyzing its po-  
 125 larization,  $s^\alpha$ , along the three Cartesian directions  $\alpha$ . Charge current along  $y$  generates a  
 126 transverse spin current parallel to  $x$  by the SHE, which results in spin accumulation at the  
 127 open lateral boundaries. The efficiency of CSI is characterized by the SHA, defined as the  
 128 ratio  $\theta_{ij}^\alpha \equiv J_{s,i}^\alpha / J_{c,j}$ , where  $\hbar \mathbf{J}_s^\alpha / 2e$  ( $\mathbf{J}_c$ ) is the spin (charge) current density,  $e$  the electron

129 charge, and  $i, j \in \{x, y\}$  denote the respective current directions. To numerically determine  
 130 the SHA, we calculated the spin accumulation response function per unit of current applied  
 131 to the lead, and fit it to the solution of the spin drift-diffusion equations:

$$\frac{s^\alpha(x)}{J_{c,y}} = -\frac{\theta_{xy}^\alpha \lambda_s^\alpha \sinh(\frac{w-2x}{2\lambda_s^\alpha})}{|e|D_s \cosh(\frac{w}{2\lambda_s^\alpha})}, \quad (2)$$

132 where  $w$  is the device width and  $D_s$  is the spin diffusion coefficient (see Supporting Infor-  
 133 mation<sup>43</sup> for details).

134 Fig. 3 shows the averaged spin accumulation along the channel cross-section,  $s^\alpha(x)$ , for  
 135 each spin orientation. In a typical SHE scenario, the electrical current, spin current, and  
 136 the spin polarization are all mutually orthogonal (for this geometry, that would generate a  
 137 finite  $s^z$  only); however, we observe a nonzero  $s^y$  as well due to the absence of a glide mirror  
 138 symmetry in 1T<sub>d</sub>-MoTe<sub>2</sub> monolayer. In fact,  $|s^z| \sim |s^y|$ , implying that the accumulated spins  
 139 point *obliquely* in the  $yz$  plane, with significant projection parallel to the electrical current.  
 140 Interestingly, note that the spin accumulation displays the hierarchy  $s^y \gtrsim s^z \gg s^x$ , echoing  
 141 the trend seen above for the spin texture and spin diffusion lengths.

142 We determine  $\theta_{xy}^\alpha$  by fitting the numerically calculated spin accumulation to Eq. (2),  
 143 using the values of  $D_s$  extracted from the two-terminal conductance of this device and  $\lambda_s^\alpha$   
 144 from Fig. 2.<sup>43</sup> The results are displayed in the inset of Fig. 3. (We note that while the charge  
 145 conductivity along  $x$  and  $y$  is slightly anisotropic, resulting in an equally anisotropic SHA,  
 146  $|\theta_{xy}^\alpha|$  and  $|\theta_{yx}^\alpha|$  are still very similar.<sup>43</sup>) At  $E_F$ , the SHA for spins pointing along  $y$  and  $z$  is  
 147  $\approx 10\%$  (with opposite sign). Remarkably, both increase substantially when approaching the  
 148 band edge, at which point  $|\theta_{xy}^y|$  slightly overcomes  $|\theta_{xy}^z|$  with values as large as  $|\theta_{xy}^y| \approx 80\%$ .  
 149 We also computed the SHC and the SHA with the Kubo formula and obtain the same result  
 150 both qualitatively and quantitatively (see Fig. 11 in Ref. <sup>43</sup>). The increase of  $\theta_{xy}$  is attributed  
 151 to hotspots of spin-Berry curvature near the bottom of the electron pockets,<sup>34,43,47</sup> which  
 152 directly determine the SHC/SHA magnitude.<sup>14,54,55</sup> Importantly, our combined results yield

153 CSI efficiencies  $\lambda_s \theta_{xy} \sim 1\text{--}50$  nm, with the largest values attained at the band edge and  
 154 for  $y$ -pointing spins. The upper limit exceeds that of traditional SOC materials (Pt,  $\beta$ -W,  
 155  $\beta$ -Ta or Au) for which  $\lambda_s \theta_{xy} \sim 0.1 - 0.2$  nm,<sup>37,39,56</sup> and is up to 2 to 3 times larger than  
 156 that induced by proximity in graphene.<sup>57–59</sup> Such remarkable CSI efficiency stems from the  
 157 combination of large spin Berry curvature *and* the persistent spin texture near the MoTe<sub>2</sub>  
 158 band edges.<sup>43</sup> These results represent the expected behavior in the monolayer limit of recent  
 159 experiments performed on few-layer MoTe<sub>2</sub><sup>33,34</sup> and WTe<sub>2</sub>.<sup>35,36</sup>

160 Such a peculiar spin response should become manifest in suitably designed nonlocal spin-  
 161 precession experiments.<sup>33,58,60,61</sup> To probe this canted SHE, we propose the device concept  
 162 pictured in the insets of Fig. 4, which relies on the reciprocal/inverse SHE (ISHE).<sup>37</sup> It  
 163 consists of a Hall bar comprising a graphene channel and a transversely aligned monolayer  
 164 TMD crystal. A non-equilibrium spin accumulation is induced in the graphene channel  
 165 through a FM electrode whose magnetization direction determines that of the spin density  
 166 injected into graphene underneath. This generates a pure-spin current that diffuses toward —  
 167 and is absorbed by — the remote TMD. It is assumed that the spin current is absorbed by  
 168 the TMD at its edge and continues to follow the diffusion direction, given that the spin  
 169 resistance in the TMD is two orders of magnitude lower than in graphene for  $\lambda_s^y = 30$  nm  
 170 or  $\lambda_s^z = 10$  nm.<sup>43</sup> By ISHE, a transverse voltage  $V_{\text{ISHE}}$  develops on the TMD, which can be  
 171 measured along its length as illustrated in Fig. 4. In experiments, the diffusing spins can be  
 172 controlled by spin precession in a non-collinear magnetic field  $B$ . To capture this situation,  
 173 we generalized the Bloch diffusion equations to account for anisotropic spin diffusion and  
 174 calculated  $V_{\text{ISHE}}(B)$  using the approach described in Ref. 58 (which accurately reproduces CSI  
 175 in real devices). Fig. 4 shows the precession response for two selected orientations of the TMD  
 176 crystal in the limit of full absorption ( $R_{\text{ISHE}} \equiv V_{\text{ISHE}}/I_0^y$ ).<sup>43</sup> We observe magnitudes of  $R_{\text{ISHE}}$   
 177 nearly three orders of magnitude larger than the values reported for graphene/TMDs<sup>57–59,62</sup>  
 178 and graphene/bulk-WSMs.<sup>33,35</sup> This is a direct consequence of the extremely large SHA  
 179 predicted here for MoTe<sub>2</sub>.<sup>63</sup>

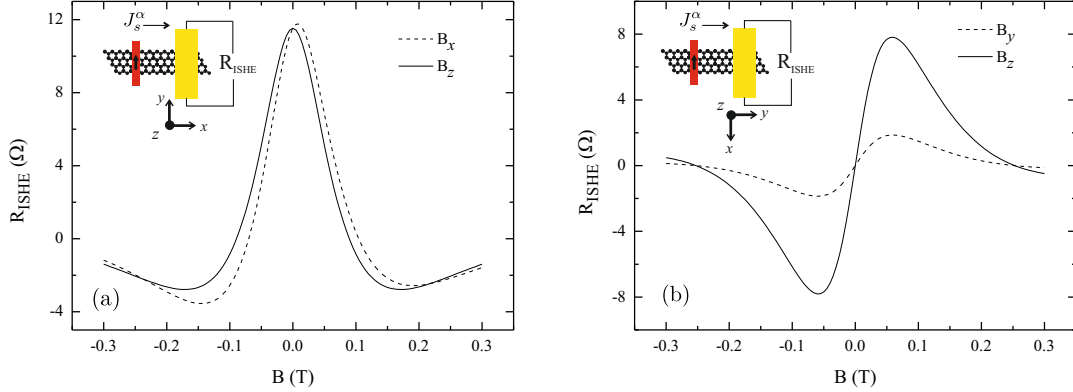


Figure 4: Simulated response of the inverse SHE ( $R_{\text{ISHE}}$ ) to spin precession for two orientations of the TMD crystal (coordinate axes in the insets). The device geometry is shown in the insets, with the TMD depicted in yellow and the FM injector in red (magnetization indicated by an arrow). The polarization of the spin current reaching the TMD ( $\mathbf{J}_s^\alpha$ ) is controlled externally with a magnetic field,  $B$ , oriented either along the graphene channel (dashed lines) or out-of-plane (solid lines). Typical experimental device dimensions were used in the simulation.<sup>43</sup>

180 The essence of the experiment is that the precession response depends strongly on the  
181 crystal orientation. As evidenced in Fig. 2, the spin relaxation in the TMD is anisotropic,  
182 and the CSI depends crucially on both the majority spin orientation and crystalline orienta-  
183 tion. In Fig. 4(a), the TMD's crystallographic  $y$ -axis is transverse to the spin propagation.  
184 A magnetic field parallel to  $z$  causes spins to precess in the graphene plane but, according to  
185 Fig. 3, only the  $y$  spin projection contributes to the ISHE signal with an efficiency of  $|\theta_{xy}^y|$ ;  
186  $R_{\text{ISHE}}$  is symmetric with respect to the sign of  $B$  because the magnetization at the FM injec-  
187 tor is parallel to  $y$ , resulting in the maximum signal at  $B = 0$ . When the field is parallel to  $x$ ,  
188 the spins acquire a  $z$  component (in addition to that in  $y$ ), which is asymmetric with respect  
189 to  $B$  and adds a contribution to the ISHE with an efficiency of  $|\theta_{xy}^z|$ ; because  $|\theta_{xy}^y| \gtrsim |\theta_{xy}^z|$ , the  
190 signal remains roughly symmetric. In Fig. 4(b), the crystallographic  $y$ -axis is parallel to the  
191 spin propagation. As the  $y$  and  $z$  directions are now orthogonal to the FM magnetization,  
192 the lineshapes are antisymmetric. The signal is zero at  $B = 0$  and, by sweeping  $B$  from  
193 negative to positive along  $z$  ( $x$ ), the spin component along  $y$  ( $z$ ) changes sign. Therefore,

194 two combined observations in this proposed experiment represent a “smoking gun” demon-  
195 stration of the intrinsic canted SHE predicted in this work: (i)  $R_{\text{ISHE}}(B)$  should display a  
196 different lineshape under different field orientations for a fixed TMD crystal; (ii) rotation of  
197 the crystal converts the lineshapes from predominantly symmetric to antisymmetric.

198 In conclusion, detailed quantum transport calculations of the spintronic response of  
199  $\text{MoTe}_2$  monolayers reveal a novel, canted SHE which reflects the unconventional spin tex-  
200 tures allowed by their reduced symmetry and strong SOC. The obtained CSI figure of merit  
201  $\lambda_s \theta_{xy} \sim 1\text{--}50$  nm is up to two orders of magnitude superior than in traditional spintronic  
202 materials such as Pt, Au, W, and Ta.<sup>37,39</sup> Given the similar electronic structures of  $\text{MoTe}_2$   
203 and  $\text{WTe}_2$ , including the persistent canted spin texture,<sup>64</sup> comparable results and efficiencies  
204 are expected in the latter, as borne out experimentally.<sup>33,34,36</sup> Our findings also call for a  
205 careful analysis of SHE measurements, since the interpretation of all-electrical detection in  
206 Hall bars<sup>34,65,66</sup> usually ignores the possibility of multiple spin Hall components. We show  
207 how the presence of canted SHE can be experimentally identified by reciprocal SHE, and  
208 how the different SHC contributions may be isolated in a spin precession setup.

## 209 **Acknowledgement**

210 M.V. acknowledges support from “La Caixa” Foundation and the Centre for Advanced 2D  
211 Materials at the National University of Singapore for its hospitality. X. W. acknowledges  
212 the ANR Flagera GRANSPORT funding. ICN2 authors were supported by the European  
213 Union Horizon 2020 research and innovation programme under Grant Agreement No. 881603  
214 (Graphene Flagship) and No. 824140 (TOCHA, H2020-FETPROACT-01-2018). ICN2 is  
215 funded by the CERCA Programme/Generalitat de Catalunya, and is supported by the Severo  
216 Ochoa program from Spanish MINECO (Grant No. SEV-2017-0706 and PID2019-111773RB-  
217 I00/ AEI / 10.13039/501100011033 ). V.M.P. acknowledges the support of the National  
218 Research Foundation (Singapore) under its Medium-Sized Centre Programme (R-723-000-

219 001-281).

## 220 References

- 221 (1) Han, W.; Otani, Y.; Maekawa, S. Quantum materials for spin and charge conversion.  
222 *npj Quantum Mater.* **2018**, *3*, 27.
- 223 (2) Manchon, A.; Železný, J.; Miron, I. M.; Jungwirth, T.; Sinova, J.; Thiaville, A.;  
224 Garelo, K.; Gambardella, P. Current-induced spin-orbit torques in ferromagnetic and  
225 antiferromagnetic systems. *Rev. Mod. Phys.* **2019**, *91*, 035004.
- 226 (3) Dolui, K.; Petrovi, M. D.; Zollner, K.; Plech, P.; Fabian, J.; Nikoli, B. K. Prox-  
227 imity SpinOrbit Torque on a Two-Dimensional Magnet within van der Waals Het-  
228 erostructure: Current-Driven Antiferromagnet-to-Ferromagnet Reversible Nonequilib-  
229 rium Phase Transition in Bilayer CrI<sub>3</sub>. *Nano Letters* **2020**, *20*, 2288–2295.
- 230 (4) Bonell, F.; Goto, M.; Sauthier, G.; Sierra, J. F.; Figueroa, A. I.; Costache, M. V.;  
231 Miwa, S.; Suzuki, Y.; Valenzuela, S. O. Control of SpinOrbit Torques by Interface  
232 Engineering in Topological Insulator Heterostructures. *Nano Letters* **2020**, *20*, 5893–  
233 5899.
- 234 (5) Fan, Y.; Wang, K. L. Spintronics Based on Topological Insulators. *SPIN* **2016**, *06*,  
235 1640001.
- 236 (6) Kononov, A.; Abulizi, G.; Qu, K.; Yan, J.; Mandrus, D.; Watanabe, K.; Taniguchi, T.;  
237 Schenberger, C. One-Dimensional Edge Transport in Few-Layer WTe<sub>2</sub>. *Nano Letters*  
238 **2020**, *20*, 4228–4233.
- 239 (7) Burkov, A. A.; Balents, L. Weyl Semimetal in a Topological Insulator Multilayer. *Phys.*  
240 *Rev. Lett.* **2011**, *107*, 127205.

- 241 (8) Wan, X.; Turner, A. M.; Vishwanath, A.; Savrasov, S. Y. Topological semimetal and  
242 Fermi-arc surface states in the electronic structure of pyrochlore iridates. *Phys. Rev. B*  
243 **2011**, *83*, 205101.
- 244 (9) Qi, Y. et al. Superconductivity in Weyl semimetal candidate MoTe<sub>2</sub>. *Nature Commu-*  
245 *nications* **2016**, *7*, 11038.
- 246 (10) Fatemi, V.; Wu, S.; Cao, Y.; Bretheau, L.; Gibson, Q. D.; Watanabe, K.; Taniguchi, T.;  
247 Cava, R. J.; Jarillo-Herrero, P. Electrically tunable low-density superconductivity in a  
248 monolayer topological insulator. *Science* **2018**, *362*, 926–929.
- 249 (11) Sajadi, E.; Palomaki, T.; Fei, Z.; Zhao, W.; Bement, P.; Olsen, C.; Luescher, S.; Xu, X.;  
250 Folk, J. A.; Cobden, D. H. Gate-induced superconductivity in a monolayer topological  
251 insulator. *Science* **2018**, *362*, 922–925.
- 252 (12) Chiu, K.-L.; Qian, D.; Qiu, J.; Liu, W.; Tan, D.; Mosallanejad, V.; Liu, S.; Zhang, Z.;  
253 Zhao, Y.; Yu, D. Flux Tunable Superconducting Quantum Circuit Based on Weyl  
254 Semimetal MoTe<sub>2</sub>. *Nano Letters (at press)* **2020**,
- 255 (13) Zhao, B.; Guo, C.; Garcia, C. A. C.; Narang, P.; Fan, S. Axion-Field-Enabled Nonre-  
256 ciprocal Thermal Radiation in Weyl Semimetals. *Nano Letters* **2020**, *20*, 1923–1927.
- 257 (14) Zhou, J.; Qiao, J.; Bournel, A.; Zhao, W. Intrinsic spin Hall conductivity of the  
258 semimetals. *Phys. Rev. B* **2019**, *99*, 60408.
- 259 (15) MacNeill, D.; Stiehl, G. M.; Guimaraes, M. H. D.; Buhrman, R. A.; Park, J.;  
260 Ralph, D. C. Control of spin-orbit torques through crystal symmetry in  
261 WTe<sub>2</sub>/ferromagnet bilayers. *Nature Physics* **2017**, *13*, 300–305.
- 262 (16) Li, P.; Wu, W.; Wen, Y.; Zhang, C.; Zhang, J.; Zhang, S.; Yu, Z.; Yang, S. A.; Man-  
263 chon, A.; Zhang, X.-x. Spin-momentum locking and spin-orbit torques in magnetic

- 264 nano-heterojunctions composed of Weyl semimetal WTe<sub>2</sub>. *Nature Communications*  
265 **2018**, *9*, 3990.
- 266 (17) Kane, C. L.; Mele, E. J. Quantum Spin Hall Effect in Graphene. *Phys. Rev. Lett.* **2005**,  
267 *95*, 226801.
- 268 (18) Kane, C. L.; Mele, E. J.  $Z_2$  Topological Order and the Quantum Spin Hall Effect. *Phys.*  
269 *Rev. Lett.* **2005**, *95*, 146802.
- 270 (19) Qian, X.; Liu, J.; Fu, L.; Li, J. Quantum spin Hall effect in two-dimensional transition  
271 metal dichalcogenides. *Science* **2014**, *346*, 1344–1347.
- 272 (20) Soluyanov, A. A.; Gresch, D.; Wang, Z.; Wu, Q.; Troyer, M.; Dai, X.; Bernevig, B. A.  
273 Type-II Weyl semimetals. *Nature* **2015**, *527*, 495–498.
- 274 (21) Sun, Y.; Wu, S.-C.; Ali, M. N.; Felser, C.; Yan, B. Prediction of Weyl semimetal in  
275 orthorhombic MoTe<sub>2</sub>. *Phys. Rev. B* **2015**, *92*, 161107.
- 276 (22) Tang, S. et al. Quantum spin Hall state in monolayer 1T'-WTe<sub>2</sub>. *Nature Physics* **2017**,  
277 *13*, 683–687.
- 278 (23) Fei, Z.; Palomaki, T.; Wu, S.; Zhao, W.; Cai, X.; Sun, B.; Nguyen, P.; Finney, J.;  
279 Xu, X.; Cobden, D. H. Edge conduction in monolayer WTe<sub>2</sub>. *Nature Physics* **2017**, *13*,  
280 677–682.
- 281 (24) Jia, Z.-Y.; Song, Y.-H.; Li, X.-B.; Ran, K.; Lu, P.; Zheng, H.-J.; Zhu, X.-Y.; Shi, Z.-  
282 Q.; Sun, J.; Wen, J.; Xing, D.; Li, S.-C. Direct visualization of a two-dimensional  
283 topological insulator in the single-layer 1T' - WTe<sub>2</sub>. *Phys. Rev. B* **2017**, *96*, 041108.
- 284 (25) Chen, P.; Pai, W. W.; Chan, Y.-H.; Sun, W.-L.; Xu, C.-Z.; Lin, D.-S.; Chou, M. Y.;  
285 Fedorov, A.-V.; Chiang, T.-C. Large quantum-spin-Hall gap in single-layer 1T'-WSe<sub>2</sub>.  
286 *Nature Communications* **2018**, *9*, 1–7.

- 287 (26) Peng, L.; Yuan, Y.; Li, G.; Yang, X.; Xian, J.-J.; Yi, C.-J.; Shi, Y.-G.; Fu, Y.-S. Ob-  
288 servation of topological states residing at step edges of WTe<sub>2</sub>. *Nature Communications*  
289 **2017**, *8*, 659.
- 290 (27) Wu, S.; Fatemi, V.; Gibson, Q. D.; Watanabe, K.; Taniguchi, T.; Cava, R. J.; Jarillo-  
291 Herrero, P. Observation of the quantum spin Hall effect up to 100 kelvin in a monolayer  
292 crystal. *Science* **2018**, *359*, 76–79.
- 293 (28) Shi, Y.; Kahn, J.; Niu, B.; Fei, Z.; Sun, B.; Cai, X.; Francisco, B. A.; Wu, D.; Shen, Z.-  
294 X.; Xu, X.; Cobden, D. H.; Cui, Y.-T. Imaging quantum spin Hall edges in monolayer  
295 WTe<sub>2</sub>. *Science Advances* **2019**, *5*.
- 296 (29) Xu, S.-Y. et al. Discovery of a Weyl fermion semimetal and topological Fermi arcs.  
297 *Science* **2015**, *349*, 613–617.
- 298 (30) Jiang, J. et al. Signature of type-II Weyl semimetal phase in MoTe<sub>2</sub>. *Nature Commu-*  
299 *nications* **2017**, *8*, 13973.
- 300 (31) Li, P.; Wen, Y.; He, X.; Zhang, Q.; Xia, C.; Yu, Z.-M.; Yang, S. A.; Zhu, Z.; Al-  
301 shareef, H. N.; Zhang, X.-X. Evidence for topological type-II Weyl semimetal WTe<sub>2</sub>.  
302 *Nature Communications* **2017**, *8*, 2150.
- 303 (32) Zhao, C.; Hu, M.; Qin, J.; Xia, B.; Liu, C.; Wang, S.; Guan, D.; Li, Y.; Zheng, H.;  
304 Liu, J.; Jia, J. Strain Tunable Semimetal–Topological-Insulator Transition in Monolayer  
305 1T′–WTe<sub>2</sub>. *Phys. Rev. Lett.* **2020**, *125*, 046801.
- 306 (33) Safeer, C. K.; Ontoso, N.; Ingla-Aynés, J.; Herling, F.; Pham, V. T.; Kurzmann, A.;  
307 Ensslin, K.; Chuvilin, A.; Robredo, I.; Vergniory, M. G.; de Juan, F.; Hueso, L. E.;  
308 Calvo, M. R.; Casanova, F. Large Multidirectional Spin-to-Charge Conversion in Low-  
309 Symmetry Semimetal MoTe<sub>2</sub> at Room Temperature. *Nano Letters* **2019**, *19*, 8758–  
310 8766.

- 311 (34) Song, P.; Hsu, C.-H.; Vignale, G.; Zhao, M.; Liu, J.; Deng, Y.; Fu, W.; Liu, Y.;  
312 Zhang, Y.; Lin, H.; Pereira, V. M.; Loh, K. P. Coexistence of large conventional and  
313 planar spin Hall effect with long spin diffusion length in a low-symmetry semimetal at  
314 room temperature. *Nature Materials* **2020**, *19*, 292–298.
- 315 (35) Zhao, B.; Khokhriakov, D.; Zhang, Y.; Fu, H.; Karpiak, B.; Hoque, A. M.; Xu, X.;  
316 Jiang, Y.; Yan, B.; Dash, S. P. Observation of charge to spin conversion in Weyl  
317 semimetal WTe<sub>2</sub> at room temperature. *Phys. Rev. Research* **2020**, *2*, 013286.
- 318 (36) Zhao, B.; Karpiak, B.; Khokhriakov, D.; Johansson, A.; Hoque, A. M.; Xu, X.;  
319 Jiang, Y.; Mertig, I.; Dash, S. P. Unconventional Charge-Spin Conversion in Weyl-  
320 Semimetal WTe<sub>2</sub>. *Advanced Materials* **2020**, *32*, 2000818.
- 321 (37) Sinova, J.; Valenzuela, S. O.; Wunderlich, J.; Back, C. H.; Jungwirth, T. Spin Hall  
322 effects. *Reviews of Modern Physics* **2015**, *87*, 1213–1260.
- 323 (38) Hoffmann, A. Spin Hall Effects in Metals. *IEEE Transactions on Magnetism* **2013**, *49*,  
324 5172–5193.
- 325 (39) Isasa, M.; Villamor, E.; Hueso, L. E.; Gradhand, M.; Casanova, F. Temperature depen-  
326 dence of spin diffusion length and spin Hall angle in Au and Pt. *Phys. Rev. B* **2015**,  
327 *91*, 024402.
- 328 (40) Laczkowski, P. et al. Large enhancement of the spin Hall effect in Au by side-jump  
329 scattering on Ta impurities. *Phys. Rev. B* **2017**, *96*, 140405.
- 330 (41) Sagasta, E.; Omori, Y.; Vélez, S.; Llopis, R.; Tollan, C.; Chuvilin, A.; Hueso, L. E.;  
331 Gradhand, M.; Otani, Y.; Casanova, F. Unveiling the mechanisms of the spin Hall effect  
332 in Ta. *Phys. Rev. B* **2018**, *98*, 060410.
- 333 (42) Seemann, M.; Ködderitzsch, D.; Wimmer, S.; Ebert, H. Symmetry-imposed shape of  
334 linear response tensors. *Phys. Rev. B* **2015**, *92*, 155138.

- 335 (43) See Supporting Information for a detailed explanation of the tight-binding model, the  
336 DFT calculations, the spin Berry curvature of the bands, the set-up for the Landauer-  
337 Büttiker and Kubo-Bastin simulations, the derivation of Eq. (2), the relation between  
338 the (persistent) spin texture and spin relaxation, the spin transport for in-gap states,  
339 the results for the  $1T'$  phase, and the modeling of the experimental detection of the  
340 canted SHE.
- 341 (44) Schliemann, J.; Egues, J. C.; Loss, D. Nonballistic Spin-Field-Effect Transistor. *Phys.*  
342 *Rev. Lett.* **2003**, *90*, 146801.
- 343 (45) Bernevig, B. A.; Orenstein, J.; Zhang, S.-C. Exact SU(2) Symmetry and Persistent  
344 Spin Helix in a Spin-Orbit Coupled System. *Phys. Rev. Lett.* **2006**, *97*, 236601.
- 345 (46) Schliemann, J. Colloquium : Persistent spin textures in semiconductor nanostructures.  
346 *Rev. Mod. Phys.* **2017**, *89*, 11001.
- 347 (47) Xu, S.-Y. et al. Electrically switchable Berry curvature dipole in the monolayer topo-  
348 logical insulator WTe<sub>2</sub>. *Nature Physics* **2018**, *14*, 900–906.
- 349 (48) Shi, L.-k.; Song, J. C. W. Symmetry, spin-texture, and tunable quantum geometry in  
350 a WTe<sub>2</sub> monolayer. *Phys. Rev. B* **2019**, *99*, 035403.
- 351 (49) Groth, C. W.; Wimmer, M.; Akhmerov, A. R.; Waintal, X. Kwant: a software package  
352 for quantum transport. *New J. Phys.* **2014**, *16*, 063065.
- 353 (50) Johnson, M.; Silsbee, R. H. Interfacial charge-spin coupling: Injection and detection of  
354 spin magnetization in metals. *Phys. Rev. Lett.* **1985**, *55*, 1790–1793.
- 355 (51) Jedema, F.; Heersche, H.; Filip, A.; Baselmans, J.; Van Wees, B. Electrical detection  
356 of spin precession in a metallic mesoscopic spin valve. *Nature* **2002**, *416*, 713–716.
- 357 (52) Fabian, J.; Matos-Abiaguea, A.; Ertler, P., C. and Stano; Žutić, I. Semiconductor Spin-  
358 tronics. *Acta Phys. Slovaca* **2007**, *57*, 565–907.

- 359 (53) Vila, M.; Garcia, J. H.; Cummings, A. W.; Power, S. R.; Groth, C. W.; Waintal, X.;  
360 Roche, S. Nonlocal Spin Dynamics in the Crossover from Diffusive to Ballistic Trans-  
361 port. *Phys. Rev. Lett.* **2020**, *124*, 196602.
- 362 (54) Sinova, J.; Culcer, D.; Niu, Q.; Sinitsyn, N. A.; Jungwirth, T.; MacDonald, A. H.  
363 Universal Intrinsic Spin Hall Effect. *Phys. Rev. Lett.* **2004**, *92*, 126603.
- 364 (55) Tanaka, T.; Kontani, H.; Naito, M.; Naito, T.; Hirashima, D. S.; Yamada, K.; Inoue, J.  
365 Intrinsic spin Hall effect and orbital Hall effect in in 4d and 5d transition metals. *Phys.*  
366 *Rev. B* **2008**, *77*, 165117.
- 367 (56) Roy, K. Estimating the spin diffusion length and the spin Hall angle from spin pumping  
368 induced inverse spin Hall voltages. *Phys. Rev. B* **2017**, *96*, 174432.
- 369 (57) Safeer, C. K.; Ingle-Aynés, J.; Herling, F.; Garcia, J. H.; Vila, M.; Ontoso, N.;  
370 Calvo, M. R.; Roche, S.; Hueso, L. E.; Casanova, F. Room-Temperature Spin Hall  
371 Effect in Graphene/MoS<sub>2</sub> van der Waals Heterostructures. *Nano Letters* **2019**, *19*,  
372 1074–1082.
- 373 (58) Benítez, L. A.; Savero Torres, W.; Sierra, J. F.; Timmermans, M.; Garcia, J. H.;  
374 Roche, S.; Costache, M. V.; Valenzuela, S. O. Tunable room-temperature spin galvanic  
375 and spin Hall effects in van der Waals heterostructures. *Nature Materials* **2020**, *19*,  
376 170–175.
- 377 (59) Herling, F.; Safeer, C. K.; Ingle-Ayns, J.; Ontoso, N.; Hueso, L. E.; Casanova, F. Gate  
378 tunability of highly efficient spin-to-charge conversion by spin Hall effect in graphene  
379 proximitized with WSe<sub>2</sub>. *APL Materials* **2020**, *8*, 071103.
- 380 (60) Savero Torres, W.; Sierra, J. F.; Benítez, L. A.; Bonell, F.; Costache, M. V.; Valen-  
381 zuela, S. O. Spin precession and spin Hall effect in monolayer graphene/Pt nanostruc-  
382 tures. *2D Mater.* **2017**, *4*, 041008.

- 383 (61) Cavill, S. A.; Huang, C.; Offidani, M.; Lin, Y.-H.; Casalilla, M. A.; Ferreira, A. Proposal  
384 for Unambiguous Electrical Detection of Spin-Charge Conversion in Lateral Spin Valves.  
385 *Phys. Rev. Lett.* **2020**, *124*, 236803.
- 386 (62) Ghiasi, T. S.; Kaverzin, A. A.; Blah, P. J.; van Wees, B. J. Charge-to-Spin Conversion  
387 by the Rashba-Edelstein Effect in Two-Dimensional van der Waals Heterostructures up  
388 to Room Temperature. *Nano Lett.* **2019**, *19*, 5959–5966.
- 389 (63) In experiments,  $R_{\text{ISHE}}$  also depends on the TMD’s electrical resistance<sup>43</sup> and the Fermi  
390 level, as seen in Fig. 3. Interfacial barriers between graphene and the TMD can suppress  
391 the spin sink effect and cause a more distributed spin absorption across the TMD width,  
392 in which case the observed signal might be partially reduced.
- 393 (64) Garcia, J. H.; Vila, M.; Hsu, C.-H.; Waintal, X.; Pereira, V. M.; Roche, S. Canted  
394 Persistent Spin Texture and Quantum Spin Hall Effect in  $\text{WTe}_2$ . *Phys. Rev. Lett.* (at  
395 *press*) **2020**,
- 396 (65) Abanin, D. A.; Shytov, A. V.; Levitov, L. S.; Halperin, B. I. Nonlocal charge transport  
397 mediated by spin diffusion in the spin Hall effect regime. *Phys. Rev. B* **2009**, *79*, 035304.
- 398 (66) Hankiewicz, E. M.; Molenkamp, L. W.; Jungwirth, T.; Sinova, J. Manifestation of the  
399 spin Hall effect through charge-transport in the mesoscopic regime. *Phys. Rev. B* **2004**,  
400 *70*, 241301.

# Figures

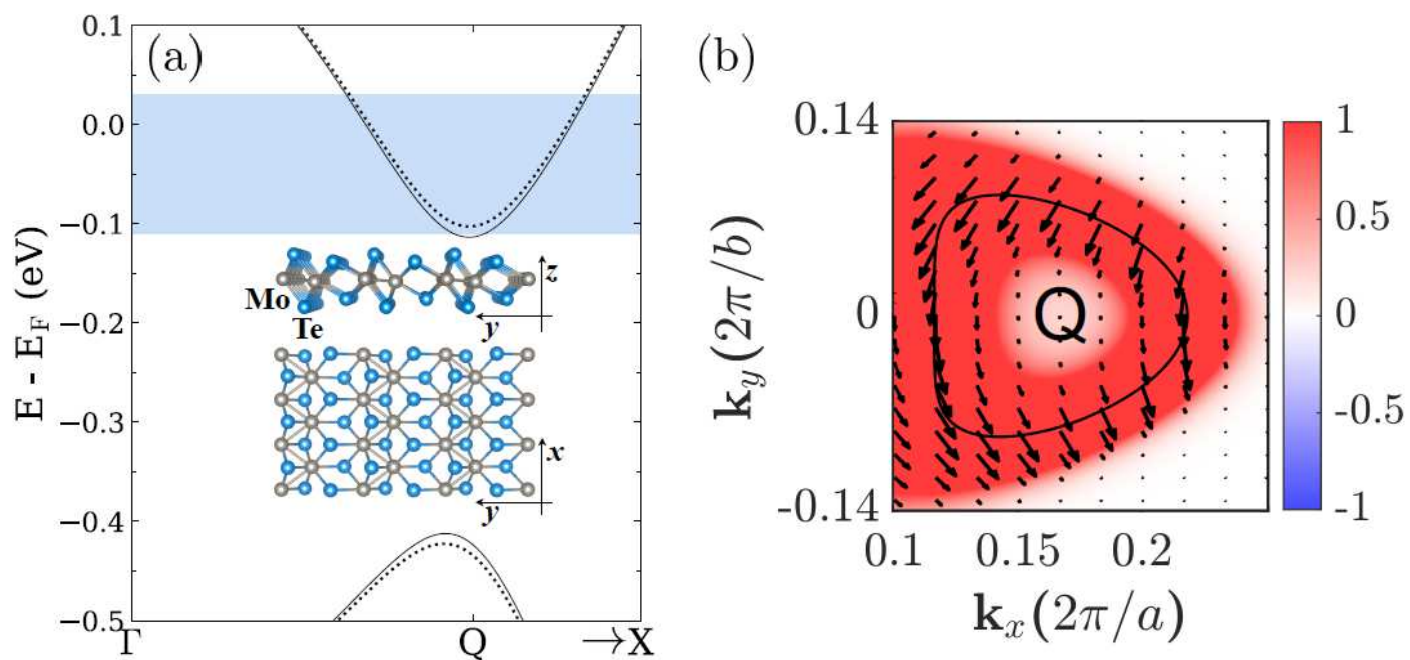
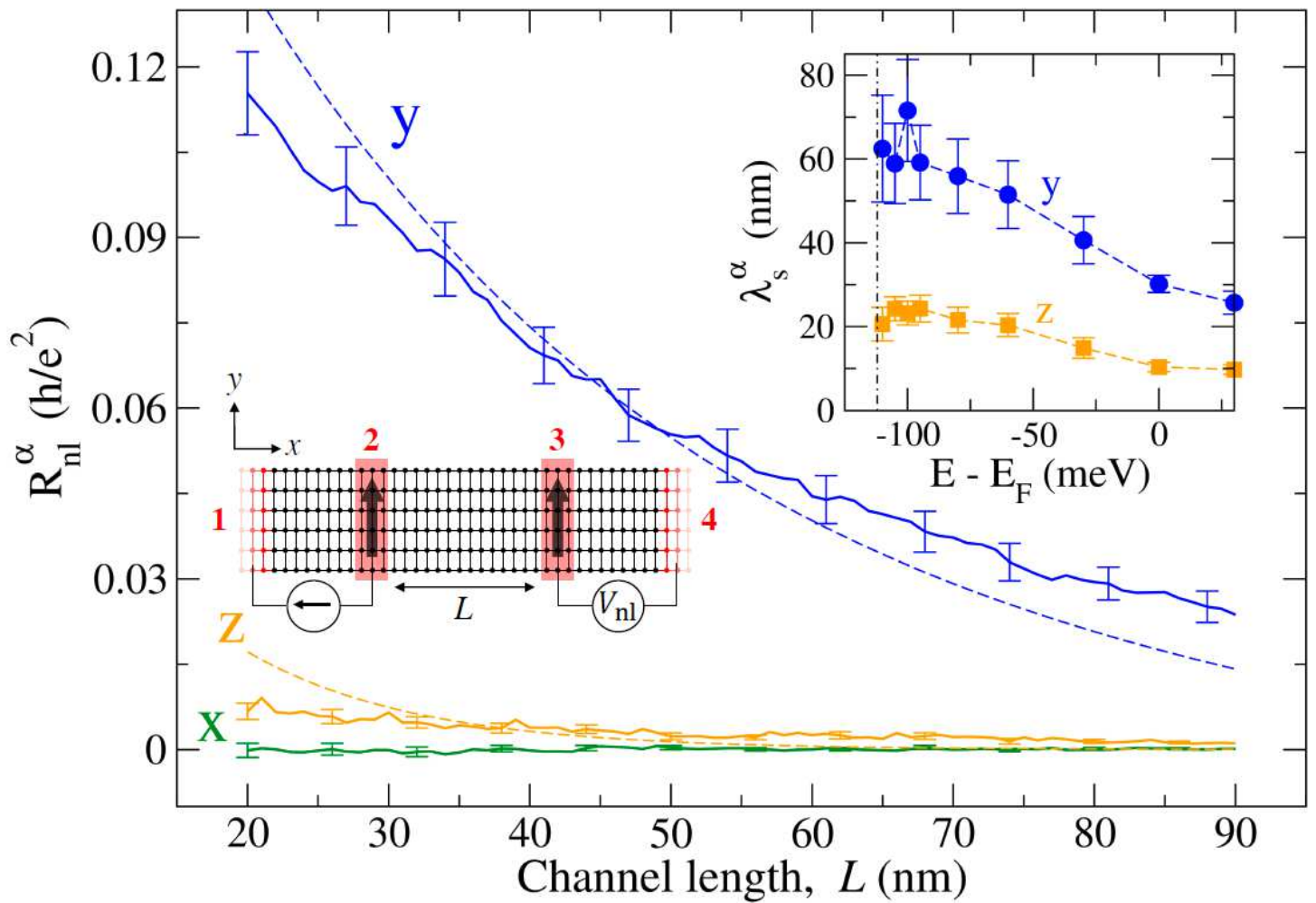


Figure 1

(a) Close-up of the bandstructure near  $E_F$  for a Td-MoTe<sub>2</sub> monolayer (model of Eq. (1)). The blue-shaded region indicates the energy range covered in the spin transport calculations. Inset: monolayer crystal structure. (b) Spin texture of one of the bands of the electron pocket near  $Q$  at  $E_F$  (Fermi-broadened with  $T = 300$  K); the solid line marks the Fermi contour, arrows depict the in-plane spin projection and the color indicates the spin projection along  $z$ .



**Figure 2**

$R_{nl}$  (solid lines) against the channel length,  $L$ , for spins polarized along  $x$ ,  $y$  and  $z$ . Error bars result from averaging over 150 disorder configurations ( $w = 50$  nm). Dashed lines are fits to Eq. (6). Left inset: Scheme of the nonlocal spin valve. Black (red) regions denote the device (leads), with leads 2 and 3 being ferromagnetic. Current  $I_0 \alpha$  flows from lead 2 to 1 and  $V_{nl}$  is measured between leads 3 and 4. Right inset: Energy-dependence of  $\lambda_{s,y,z}$ . The dot-dashed line marks the conduction band minimum.

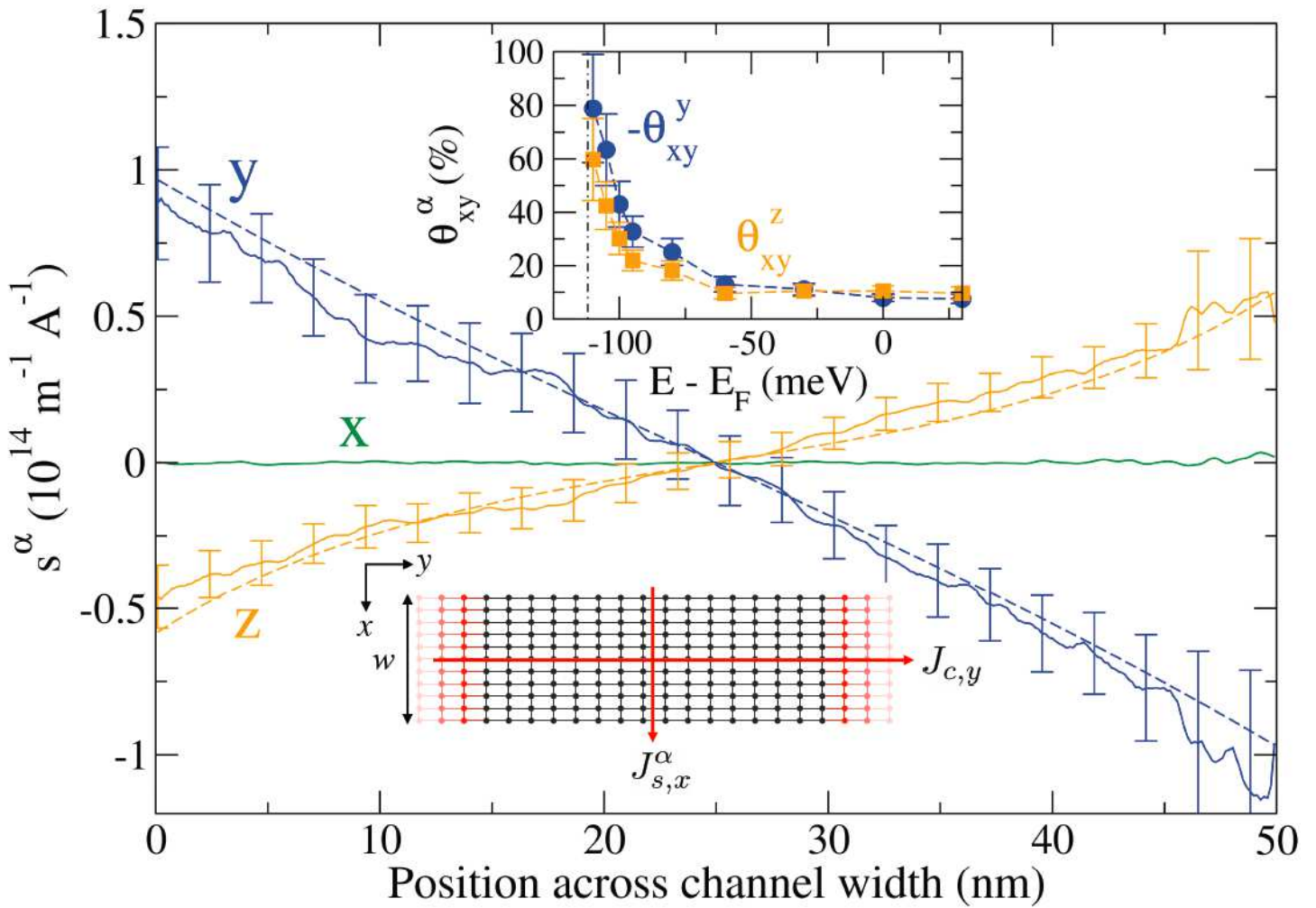


**Figure 3**

Spin accumulation (solid lines) as a function of position across the channel width, of spins along x, y and z. Error bars result from averaging over 200 disorder configurations ( $w = 50$  nm). Dashed lines are fits to Eq. (2). Bottom inset: Scheme of the two-terminal device, where a current flowing along y creates a spin accumulation in the x direction. Top inset: Energy dependence of the spin Hall angles, with the conduction band minimum marked by a dot-dashed line.

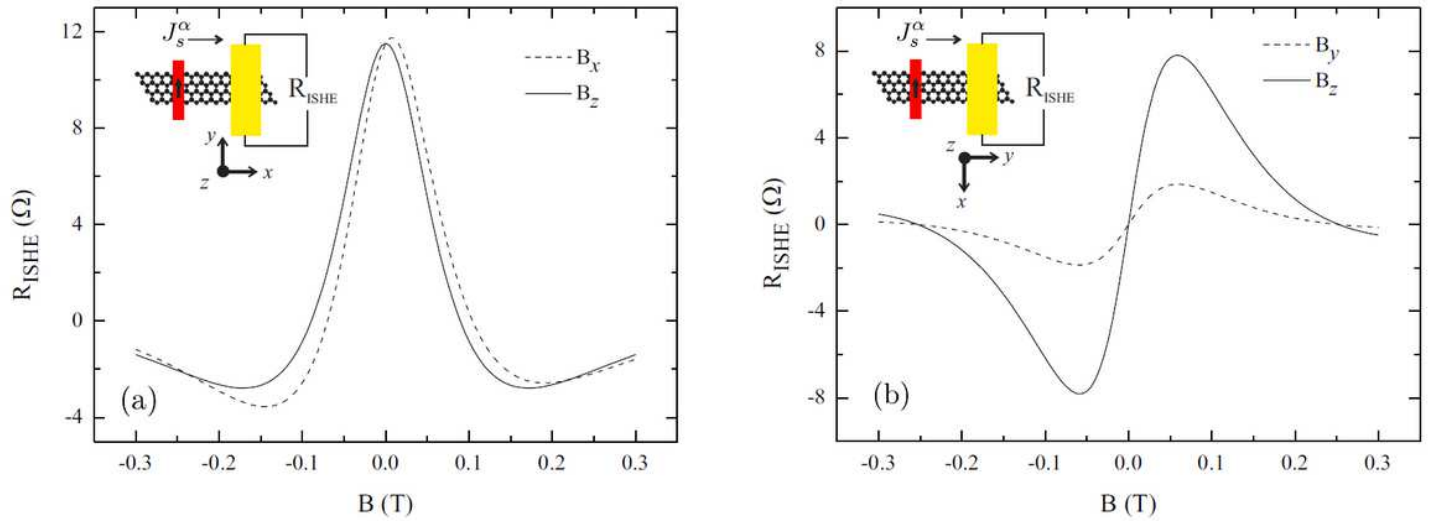


**Figure 4**

Simulated response of the inverse SHE (RISHE) to spin precession for two orientations of the TMD crystal (coordinate axes in the insets). The device geometry is shown in the insets, with the TMD depicted in yellow and the FM injector in red (magnetization indicated by an arrow). The polarization of the spin current reaching the TMD ( $J_s^\alpha$ ) is controlled externally with a magnetic field,  $B$ , oriented either along the graphene channel (dashed lines) or out-of-plane (solid lines). Typical experimental device dimensions were used in the simulation.<sup>43</sup>

## Supplementary Files

This is a list of supplementary files associated with this preprint. Click to download.

- [Suppinfo.pdf](#)